10

Temperature Measurements with Lidar

Andreas Behrendt

Universität Hohenheim, Institut für Physik und Meteorologie, Garbenstraße 30, D-70599 Stuttgart, Germany (behrendt@uni-hohenheim.de)

10.1 Introduction

Temperature is a key parameter of the state of the atmosphere. Temperature data play an important role in such fields as atmospheric dynamics, climatology, meteorology, and chemistry, to name just a few. In addition to these direct geophysical applications, the atmospheric temperature profile is necessary as an input parameter to many remote-sensing techniques including lidar for the determination of other quantities. Examples are the measurement of the particle backscatter and particle extinction coefficients with Raman lidar [1], particle polarization [2], water-vapor mixing ratio with Raman lidar [3], or the measurement of trace-gas concentrations with differential-absorption lidar. Until now, temperature profiles of a model atmosphere or the results of radiosonde soundings (in the free troposphere and lower stratosphere) have usually been taken for this purpose. It is obvious that the quality of the results is considerably improved when the atmospheric temperature profile is measured at the same location during the same time interval.

10.2 Overview on Temperature Lidar Techniques

Today, lidar techniques for the remote sensing of atmospheric temperature profiles have reached the maturity necessary for routine observations. Stable and rugged systems have been employed successfully and advanced the understanding of atmospheric processes and climatology. At present, there are three lidar techniques available for

routine observations. Together, they cover a height range from the ground to the lower thermosphere: rotational Raman (for observations from the ground to the upper stratosphere), the integration technique (from the lower stratosphere up to the mesopause), and the resonance fluorescence technique (from the mesopause region to the lower thermosphere). As any optical measurement in the atmosphere that does not depend on the sun or some other celestial object as a radiation source, these techniques work best at nighttime when the background noise is low. However, high-power systems with spectrally narrow signal detection have to date been set up that also perform well under daytime conditions. Other lidar techniques for temperature profiling are under development such as high-spectral resolution lidar (HSRL) and differential absorption lidar (DIAL).

In this chapter, lidar techniques for temperature-profile measurements are reviewed. The reader will find a detailed description of integration lidar and rotational Raman lidar. The remaining techniques for lidar temperature profiling are covered in detail in other chapters of this book: the resonance fluorescence technique in Chapter 11, the HSRL technique in Chapter 5 and temperature measurements with DIAL in Chapter 8. An overview of the techniques presently available for temperature profiling with lidar is given in Table 10.1.

The integration technique uses a molecular backscatter signal. This signal can be either the Rayleigh band, the Cabannes line (sometimes also called "Rayleigh line"), a temperature-independent fraction of the pure rotational Raman band, a vibrational Raman band or line, or part of the central ("Gross") Brillouin line. The intensity of a molecular lidar signal is proportional to the number density N of atmospheric molecules at height z, $N(z)$. Under the assumption that the atmosphere is in hydrostatic equilibrium and with the initialization at a reference height, the temperature profile can be derived from $N(z)$ and the ideal-gas law. To extend the height range of the integration technique downward below $\sim$30 km where particles are present in quantities sufficient to severely perturb Rayleigh integration lidar, an inelastic lidar such as the vibrational Raman signal of N_2 can be used instead of the Rayleigh signal [4–6]. However, when aerosol extinction becomes significant compared with molecular extinction, this technique also fails.

Here rotational Raman (RR) lidar is the method of choice. With RR lidar, temperature measurements can be carried out not just in the clear atmosphere, but in aerosol layers and optically thin clouds as well. The technique is based on the fact that the intensities of the

Table 10.1. Overview of the lidar techniques for atmospheric temperature profiling. The height ranges are for the systems which were most advanced at the time of writing

Technique	Principle	Comments
Integration technique with elastic (Rayleigh or Cabannes) backscatter signal	• Molecular lidar signal is proportional to molecular number density • Hydrostatic equilibrium is assumed	• For measurements between ~30 and ~100 km • Observed height region must be free from particles
Integration technique with inelastic (Raman or Brillouin) backscatter signal	Same as above	• For measurements in the stratosphere • Can handle particle backscattering but no significant particle extinction
Rotational Raman technique	• Temperature dependence of the intensities of rotational Raman lines • Ratio of two signals	• For measurements in the troposphere and stratosphere • Measurements in clouds possible (details see text)
Brillouin–Doppler technique (HSRL ratio)	• Temperature dependence of the Doppler broadening of the Brillouin band • Ratio of two signals	• For measurements in the troposphere • Measurements in thin clouds possible
DIAL	• Temperature dependence of the strength of molecular absorption lines	• Feasibility demonstrated, first experimental data in boundary layer available • Difficulties in handling gradients of particle backscattering
Resonance fluorescence	• Temperature dependence of the Doppler broadening of resonance fluorescence of metal atoms • Ratio of two signals	• High-resolution measurements in heights were metal atoms are present with high mixing ratio, i.e., ~75 km to 120 km

HSRL: High spectral resolution lidar (note that the integration technique with the use of a Brillouin signal is also called HSRL in the literature and must be distinguished from the HRSL ratio technique); DIAL: differential absorption lidar.

lines within the pure rotational Raman band exhibit different dependencies on temperature. The intensities of lines close to the incident laser line decrease with rising temperature, while the intensities of lines with large wavelength differences increase. This feature is a result of the population of rotational energy levels which is described by a

Maxwell–Boltzmann distribution. With the ratio of two RR lidar signals of opposite temperature dependence, one has a quantity with a temperature dependence that is independent of atmospheric transmission and range. In contrast to the integration technique, the RR technique does not use the assumption that the atmosphere is in hydrostatic equilibrium. Thus, even in turbulent layers no systematic measurement errors occur. In addition, as inelastic lidar signals, i.e., signals at wavelengths different from the laser wavelength are used, the rotational Raman technique can also be applied in heights in which particles are present because the backscatter signal of particles has the same wavelength as the laser. However, for RR lidar measurements in clouds to produce reliable results, the transmission of elastic-backscatter light in the rotational Raman channels must be very low ($<10^{-7}$). As the rotational Raman line signals are only a few nm apart from the laser wavelength, the realization of such a system was quite an instrumental challenge. The problem is solved today using state-of-the art optical components in the receiver.

The Brillouin–Doppler technique (see Chapter 5), also called "Rayleigh–Doppler technique" or "high-spectral-resolution lidar (HSRL) ratio technique," uses the temperature dependence of the width, i.e., Doppler broadening, of the Cabannes line. Meanwhile, temperature measurements up to the lower stratosphere can be made with this technique using iodine vapor absorption cells of different temperatures to reject the elastic particle signal and to obtain two molecular lidar signals of different dependence on atmospheric temperature [7].

Also, differential absorption lidar (DIAL, see Chapter 8) can be used for temperature measurements. The temperature-dependent absorption of O_2 lines in the near infrared is used for this purpose. Simulations, however, reveal that it is difficult to deal with the effect of Doppler-broadening of the Rayleigh backscatter signals with sufficient accuracy [8].

Finally, lidar temperature measurements around the mesopause and in the lower thermosphere are based on the Doppler-broadened lineshape of resonance fluorescence from atoms of metals such as Na, Ca, K, Fe which are present in varying concentrations between ~75 and 120 km height (see Chapter 11). The large backscatter cross section of resonance fluorescence and the absence of particle scattering at these altitudes make the technique highly reliable. Daytime operation is possible by using, e.g., Faraday cells in the receiver which act as ultranarrowband filters to exclude the sunlight and only transmit the lidar return signals.

10.3 The Integration Lidar Technique

10.3.1 Theory

A profile of the spatial density $N(z)$ of atmospheric molecules can be derived from the elastic lidar return signal $S(z)$ by rearranging the lidar equation, yielding

$$N(z) = \frac{C\, S(z)\, (z - z_0)^2}{\tau(z_0, z)^2}. \tag{10.1}$$

Here z_0 is the altitude of the lidar above sea level. C includes all atmospheric and instrumental parameters that are constant with height during the time of the measurement. C also includes the extinction of the lidar signal in as far as it is due to particles and clouds; when defining C in this way, it is tacitly assumed that the integration from which the method borrows its name (see below) is carried out at elevations well above that part of the atmosphere in which clouds and aerosols are present. $\tau(z_0, z)^2$ is the atmospheric roundtrip molecular transmission between the lidar and the measurement height z. C depends on the lidar system (laser power, receiver telescope area, receiver efficiency), on the type of signal detected (Rayleigh, Cabannes, Raman), the height resolution of the measured data, and the particle load of the atmosphere. As C is unknown and difficult to determine accurately enough, only a relative density profile can be deduced from the lidar data alone. To obtain absolute density values, C is quantified by normalizing $N(z)$ either to a climatological model atmosphere or to radiosonde data at a reference height $z_{\mathrm{ref},1}$ that must be higher than all particle-containing height regions:

$$N(z) = \frac{N(z_{\mathrm{ref},1}) \quad S(z) \quad (z - z_0)}{S(z_{\mathrm{ref},1})\, \tau(z_{\mathrm{ref},1}, z)^2\, (z_{\mathrm{ref},1} - z_0)^2}, \tag{10.2}$$

where $\tau(z_{\mathrm{ref},1}, z)$ is the atmospheric transmission between $z_{\mathrm{ref},1}$ and z. However, as will be explained below, temperature measurements with the integration technique do not require the density profile itself but only the density ratio in two successive range bins.

If a Raman lidar signal is used for the temperature measurement, the difference in wavelength is accounted for by using $\tau(\lambda_0, z_0, z)\, \tau(\lambda', z_0, z)$, with λ_0 for the laser wavelength and λ' for the wavelength of the Raman signal, instead of $\tau(\lambda_0, z_0, z)^2$ or, as had been written for simplicity in Eqs. (10.1) and (10.2), $\tau(z_0, z)^2$. For $\tau(\lambda_0, z_0, z)$ usually

one factor for the extinction of the signal due to Rayleigh scattering,

$$\tau_{\mathrm{Ray}}(\lambda, z_0, z) = \exp\left(-\sigma_{\mathrm{Ray}}(\lambda) \int_{z_0}^{z} N(\zeta)\mathrm{d}\zeta\right), \tag{10.3}$$

and one factor for ozone absorption,

$$\tau_{\mathrm{ozone}}(\lambda, z_0, z) = \exp\left(-\sigma_{\mathrm{ozone}}(\lambda) \int_{z_0}^{z} N_{\mathrm{ozone}}(\zeta)\mathrm{d}\zeta\right), \tag{10.4}$$

are sufficient, since the laser wavelength used for integration lidar is normally not absorbed by other atmospheric molecules. $N_{\mathrm{ozone}}(z)$ can be taken, e.g., from radiosoundings, lidar measurements, or a model atmosphere. When inserting Eqs. (10.3) and (10.4) into Eq. (10.2), the resulting equation cannot be solved analytically for $N(z)$, thus the atmospheric density in the transmission term of Eq. (10.3) is as a rule approximated with data from a climatological model atmosphere. This procedure does normally not cause large errors. It is also possible to minimize the influence of model data at this point of the algorithm by an iterative approach: using the resulting $N(z)$ of a first calculation as the input for the next yields a better second approximation, etc.

The temperature profile is derived from $N(z)$ by making use of the ideal-gas law

$$p(z) = k\, N(z)\, T(z) \tag{10.5}$$

with the pressure $p(z)$, Boltzmann constant k, and temperature $T(z)$ and with the barometric height formula

$$\mathrm{d}p(z) = -\rho(z)\, g(z)\, \mathrm{d}z \tag{10.6}$$

which is valid for the atmosphere under the condition of hydrostatic equilibrium.

$$\rho(z) = N(z)M \tag{10.7}$$

is the atmospheric density with M as the average molecular mass of the atmospheric constituents. The mixing ratio of the major atmospheric constituents N_2, O_2, and Ar can be considered as constant at least up to the mesopause. Above, a small correction for the decrease of M with height is recommended. Equations (10.5)–(10.7) result in

$$T(z) = \frac{N(z_{\mathrm{ref},2})}{N(z)} T(z_{\mathrm{ref},2}) + \frac{M}{kN(z)} \int_{z_{\mathrm{ref},2}}^{z} g(\zeta)N(\zeta)\mathrm{d}\zeta. \tag{10.8}$$

Thus, with the input of $N(z_{\mathrm{ref},2})$ and $T(z_{\mathrm{ref},2})$, the temperature profile $T(z)$ can be derived in successive steps starting at the reference height $z_{\mathrm{ref},2}$:

$$T(z_{i+1}) = \frac{N(z_i)}{N(z_{i+1})} T(z_i) + \frac{M}{kN(z_{i+1})} \bar{g} \bar{N} \Delta z. \tag{10.9}$$

Here z_i, z_{i+1} are the center heights of successive range bins of the lidar data,

$$\Delta z = z_{i+1} - z_i, \tag{10.10}$$

and $\bar{g}$ and $\bar{N}$ are the acceleration of gravity and molecular density, respectively, averaged between z_i and z_{i+1}.

For $\bar{g}$ the approximation

$$\bar{g} = g(z_i + z_{i+1})/2 \tag{10.11}$$

is appropriate, whereas for $\bar{N}$ the exponential dependence of $N(z)$ with height must be taken into account, a linear fit would result in significant measurement errors. Using the approximation

$$N(z) = N(z_i) \exp(-b(z - z_i)) \Rightarrow N(z_{i+1}) = N(z_i) \exp(-b\Delta z), \tag{10.12}$$

where b is a constant, yields

$$\bar{N} = \int_{z_i}^{z_{i+1}} \frac{N(\zeta)}{\Delta z} \mathrm{d}\zeta = \frac{N(z_i) - N(z_{i+1})}{b\Delta z}. \tag{10.13}$$

Since from Eq. (10.12) we have

$$\ln(N(z_{i+1})/N(z_i)) = -b\Delta z, \tag{10.14}$$

we get

$$\bar{N} = \frac{N(z_i) - N(z_{i+1})}{\ln(N(z_i)/N(z_{i+1}))}. \tag{10.15}$$

Thus, Eq. (10.9) can finally be written as

$$T(z_{i+1}) = \frac{N(z_i)}{N(z_{i+1})} T(z_i) + \frac{Mg((z_i + z_{i+1})/2)}{k} \Delta z \frac{(N(z_i)/N(z_{i+1})) - 1}{\ln(N(z_i)/N(z_{i+1}))}. \tag{10.16}$$

It is noteworthy that only the relative value of $N(z)$ is used in Eq. (10.16) and $T(z)$ is therefore independent of the normalization of the density profile at $z_{\mathrm{ref},1}$ in a first-order approximation, i.e., when a model atmosphere is used to calculate the Rayleigh extinction of the signal in Eq. (10.3).

In principle, the reference altitude $z_{\mathrm{ref},2}$ can be chosen at the upper or at the lower boundary of the altitude range in which the integration-technique measurements are made. The data are then derived successively downward or upward, respectively. However, $T(z_{\mathrm{ref},2})N(z_{\mathrm{ref},2})$ must be highly accurate if profiles are to be generated upward because errors build up exponentially. On the other hand, when an upper reference height is chosen and the data are derived downward, errors in $T(z_{\mathrm{ref},2})N(z_{\mathrm{ref},2})$ become quickly smaller. Due to this, $T(z_{\mathrm{ref},2})$ and $N(z_{\mathrm{ref},2})$ are usually taken at the upper boundary of the lidar data, e.g., from a climatological model atmosphere or from collocated measurements with other instruments like resonance fluorescence lidar or airglow imagers.

Errors which are caused by the initialization with $T(z_{\mathrm{ref},2})N(z_{\mathrm{ref},2})$ were investigated, e.g., by Leblanc et al. [9] for downward integration. The authors used simulated data which were 15 K above the model atmosphere for all heights and found that the 15-K initialization error at 90 km decreased to 4 K at 80 km and to 1 K at 70 km. For real measurements the reference-height value should be much closer to the correct data than in this worst-case scenario so the actual downward-integration errors should be considerably smaller. It must be noted in this context that, when altitude-dependent signal-induced noise is present in the signals, inaccurate background subtraction can cause large errors. Signal-induced noise, when present, must be identified, and the data must be corrected.

The pressure profile $p(z)$ is related to $N(z)$ and $T(z)$ via Eq. (10.5). Other formalisms which derive first a pressure profile and then the temperature profile [10] are equivalent to the algorithm discussed here.

10.3.2 Applications

Atmospheric temperature profiling with the lidar integration technique started in pre-laser times. As early as 1953, Elterman utilized a searchlight to obtain molecular density profiles. Via initialization with radiosonde data and the use of "physically acceptable" lapse rates,

he obtained temperature profiles up to 67.6 km [11, 12] and studied seasonal trends of temperature, density, and pressure [13]. First measurements with laser light were done in the 1960s with a Q-switched ruby laser by Sanford and reported in an early review paper [14]. At the beginning of the 1970s, pioneering integration-technique measurements with inelastic signals were carried out by Fiocco et al. [15]. These authors used a single-mode continuous-wave argon-ion laser to measure temperature and backscatter ratio in the troposphere. The particle backscattering contribution to the molecular signal was reduced with a Fabry–Perot interferometer. Later attempts to measure temperature profiles with Cabannes scattering and to block the particle backscatter signal with a Michelson interferometer did not succeed [16]. With the use of broadband dye lasers (which were originally developed for Na and Li density measurements in the mesosphere) Hauchecorne and Chanin obtained the first lidar temperature profiles between 35 and 70 km height [10] by detecting the Rayleigh backscatter signal from the middle atmosphere. In these altitudes there are virtually no particles present which at low heights perturb the measurements. Following this breakthrough, better-suited laser types like frequency-doubled Nd:YAG [17] and excimer lasers [18] were soon employed. In the following years, the high precision of these measurements which did not need to be calibrated and the ease of implementation of the technique on existing lidar systems started the study of a wide range of geophysical phenomena. These included gravity waves [19–22], stratospheric warming and planetary waves [23, 24], semi-diurnal and diurnal thermal tides [25–29], mesospheric inversions [30, 31], the oscillation of the 27-day solar cycle [32], the influence of the 11-year solar cycle [33, 34], climatology [35, 36], and long-term trends [37]. To ensure the quality of the measured data, sources of possible errors were investigated in detail [9, 38]. Rayleigh lidar systems serve today to evaluate and validate middle-atmosphere temperature measurements from satellites and are core instruments in the Network for the Detection of Stratospheric Change (NDSC).

10.4 Rotational Raman Lidar

10.4.1 Brief Historical Survey

The use of RR backscatter signals for atmospheric temperature profiling with lidar was originally proposed in 1972 by Cooney [39]. First

boundary-layer measurements were made with interference filters in the 1970s [40, 41] and later also with grating spectrometers [42]. With subsequent improvements in laser and receiver technology, the measurement range could be extended into the stratosphere [43, 44] and semi-automated, quite robust systems for tropospheric profiling were set up [45]. Advances in interference filter manufacturing allow today the design of receiver systems with very low losses in the separation of the lidar signals and massive reduction of the elastic backscatter crosstalk so measurements can be made even in clouds with a backscatter ratio of more than 50 without the need for corrections [46]. These systems can be built sufficiently rugged to work reliably under harsh conditions during field campaigns. The temporal resolution of today's most powerful systems is a few minutes within the troposphere at a height resolution of $\sim$100 m and a measurement uncertainty of $\sim\pm$1 K [47, 48]. The measurement range of these instruments extends up to the stratopause region for night-integrated observations. As an alternative to interference filters, double-grating spectrometers are also in use today which yield similar blocking power at slightly lower cost but also have lower receiver efficiency. A high-power interference-filter-based system can also measure in the daytime [47]. To improve the daytime performance, either a transmitter that emits at short wavelengths in the solar-blind spectral region [49] or a narrow-field-of-view receiver can be used. Furthermore, the spectural bandwidth of the receiver can be narrowed by separating the N_2 RR lines by means of a Fabry–Perot interferometer (FPI) [50]. A first attempt using UV radiation from a narrow-band Raman-shifted KrF excimer laser and a thallium atomic vapor filter to block the elastic backscatter signal yielded measurements up to 1800 m height, but with large deviations of $\pm$10 K [51] from the data of a local radiosonde. The approach using an FPI succeeded in measurements throughout the troposphere with results very close to the data of a reference sonde [52]. The RR technique can conveniently be combined with other lidar techniques, thus allowing the setup of multiparameter Raman lidar systems. Standard laser sources with high emission power can be used with—as the only non-standard feature—frequency stabilization by injection seeding; this is very helpful for obtaining a stable calibration function. RR lidars have been used successfully for the investigation of a number of geophysical phenomena. One of the first and which is still in progress was the formation of polar stratospheric clouds in the arctic winter [53, 54]; here the unique capability of RR lidar to allow continuous monitoring of optical

particle properties and temperature in the same air masses proves highly beneficial.

10.4.2 Theory

In this section, a summary of the equations that describe the intensity of the atmospheric rotational Raman (RR) backscattering is given. The theory of Raman scattering is described in more detail in Chapter 9.

For simulation studies of RR temperature lidar, it is generally sufficient to consider air as a constant mixture of nitrogen and oxygen with relative volume abundances of 0.7808 and 0.2095, respectively. The remaining gases need not be considered. This also applies to water vapor. Its RR cross section is not much larger than the cross sections of N_2 and O_2 [55], but its relative amount is quite low even in conditions of water vapor saturation. Nitrogen and oxygen molecules can be treated here as simple linear molecules (SLM), i.e., linear molecules with no electronic momentum coupled to the scattering.

The rotational energy $E_{\mathrm{rot},i}(J)$ of a homonuclear diatomic molecule (like molecular nitrogen and oxygen) in the rotational quantum state J is [56]

$$E_{\mathrm{rot},i}(J) = [B_{0,i}J(J+1) - D_{0,i}J^2(J+1)^2]hc,\ J = 0, 1, 2, \ldots, \tag{10.17}$$

where h is Planck's constant, c is the velocity of light, and i denotes the atmospheric constituent. $B_{0,i}$ and $D_{0,i}$ are the rotational constant and centrifugal distortion constant for the ground state vibrational level. On the frequency scale, the shift of the rotational Raman lines is independent of the wavelength of the exciting light λ_0. For the Stokes branch it is given by

$$\Delta\nu_{\mathrm{St},i}(J) = -B_{0,i}2(2J+3) + D_{0,i}[3(2J+3) + (2J+3)^3],$$
$$J = 0, 1, 2, \ldots \tag{10.18}$$

and for the anti-Stokes branch by

$$\Delta\nu_{\mathrm{ASt},i}(J) = B_{0,i}2(2J-1) - D_{0,i}[3(2J-1) + (2J-1)^3] \quad \text{with}$$
$$J = 2, 3, 4, \ldots. \tag{10.19}$$

The differential backscatter cross section for single lines of the pure rotational Raman spectrum can be written as [57]

$$\left(\frac{\mathrm{d}\sigma}{\mathrm{d}\Omega}\right)_{\pi}^{\mathrm{RR},i}(J) = \frac{112\pi^4}{15}\frac{g_i(J)\,h\,c\,B_{0,i}(\nu_0 + \Delta\nu_i(J))^4\,\gamma_i^2}{(2I_i+1)^2\,k\,T} \times X(J)\exp\left(-\frac{E_{\mathrm{rot},i}(J)}{kT}\right) \tag{10.20}$$

where for the Stokes branch

$$X(J) = \frac{(J+1)(J+2)}{2J+3} \quad \text{with} \quad J = 0, 1, 2, \ldots \tag{10.21}$$

and for the anti-Stokes branch

$$X(J) = \frac{J(J-1)}{2J-1} \quad \text{with} \quad J = 2, 3, 4, \ldots . \tag{10.22}$$

$g_i(J)$ is the statistical weight factor which depends on the nuclear spin I_i. ν_0 denotes the frequency of the incident light, γ_i is the anisotropy of the molecular polarizability tensor, k is Boltzmann's constant and T is temperature. Equation (10.20) is valid if both polarization components of the RR signals are detected with the same efficiency in the lidar receiver. The depolarization of the pure rotational Raman wings is 3/4 [55], i.e., for linearly polarized incident light, a fraction of 4/7 of the backscatter signal intensity is polarized parallel and 3/7 perpendicular to the polarization plane of the incident light. To provide high signal intensities, RR lidars are usually designed to detect both polarization components with high efficiency.

The number of photons detected in an RR channel can be calculated with

$$S_{\mathrm{RR}}(z) = S_0\varepsilon\frac{A\,O(z)}{(z-z_0)^2}\Delta z N(z)\left[\sum_{i=\mathrm{O_2,N_2}}\sum_{J_i}\tau_{\mathrm{RR}}(J_i)\eta_i\left(\frac{\mathrm{d}\sigma}{\mathrm{d}\Omega}\right)_{\pi}^{\mathrm{RR},i}(J_i)\right] \times \tau_{\mathrm{atm}}(z_0,z)^2 \tag{10.23}$$

where S_0 is the number of transmitted photons, ε is the detector efficiency, A is the free telescope area, $O(z)$ describes the overlap between transmitted laser beam and telescope, Δz is the height resolution, $N(z)$ is the spatial density of air molecules, $\tau_{\mathrm{RR}}(J_i)$ is the transmission of the receiver at the wavelength of the RR line J_i, η_i is the relative

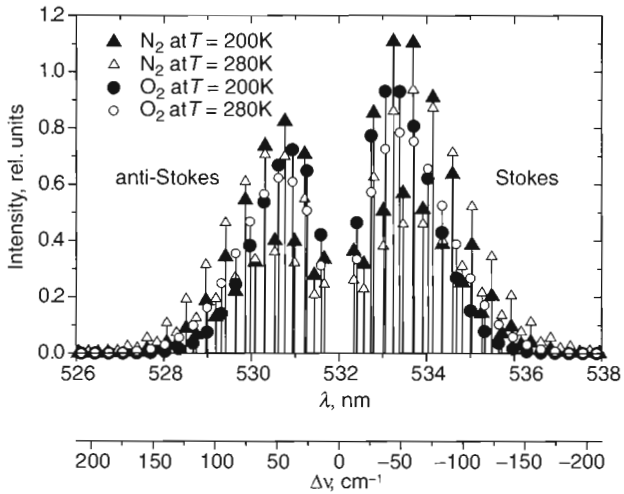

Fig. 10.1. Pure rotational Raman spectrum of air calculated for temperatures of $T = 200\,\mathrm{K}$ and $T = 280\,\mathrm{K}$ (intensity in relative units). The wavelength scale is for a laser wavelength of 532 nm.

volume abundance of N_2 and O_2, respectively, and $\tau_{\mathrm{atm}}(z_0, z)^2$ is the atmospheric roundtrip transmission.

Figure 10.1 shows the pure rotational Raman spectrum of air calculated for two temperatures, 200 and 280 K. The values employed for $B_{0,i}$, $D_{0,i}$, $g_i(J)$, I_i, and γ_i^2 are listed in Table 10.2. For simplicity, the cgs units used by the authors are quoted. In Chapter 9 it is shown how these values can be transformed into the SI system. γ_i depends weekly on wavelength [$\gamma_{O_2}(\lambda = 488\,\mathrm{nm})/\gamma_{O_2}(\lambda = 647.1\,\mathrm{nm}) = 1.17 \pm 11\%$; $\gamma_{N_2}(\lambda = 488\,\mathrm{nm})/\gamma_{N_2}(\lambda = 647.1\,\mathrm{nm}) = 1.13 \pm 11\%$] and is considered as constant with temperature in this context [57].

Table 10.2. Ground-state rotational and centrifugal distortion constants $B_{0,i}$ and $D_{0,i}$, statistical weight factors $g_i(J)$, nuclear spin I_i, and the square of the anisotropy of the molecular polarizability tensor γ_i^2.

Molecule	$B_{0,i}$ (cm^{-1})	$D_{0,i}$ (cm^{-1})	$g_i(J)$		I_i	γ_i^2 (cm^6)
			J even	J odd		
N_2	1.98957 [60]	5.76×10^{-6} [60]	6	3	1	0.51×10^{-48} [61]
O_2	1.43768 [56]	4.85×10^{-6} [56]	0	1	0	1.27×10^{-48} [61]

For RR temperature lidar the splitting of the O_2 RR lines in triplets [58] can be neglected because the two satellite lines located close to the main lines, at distances of 0.056 nm on either side, have intensities of only about 3% of the intensity of each central line. Pressure broadening of the RR lines [43] can also be disregarded when the transmission bands of the filters are broad compared to the width of the lines, which is ~2 GHz. (With a suitable narrow-band receiver, however, one could also make use of the pressure broadening and measure temperature and pressure simultaneously [59].)

For atmospheric temperature profiling with the rotational Raman technique, usually the ratio

$$Q(T,z) = \frac{S_{\mathrm{RR2}}(T,z)}{S_{\mathrm{RR1}}(T,z)} \tag{10.24}$$

is used with S_{RR1} and S_{RR2} for two pure-rotational Raman signals of opposite temperature dependence. (One can also combine the signals in other ways which, however, gives no advantages.) In the ratio, altitude-dependent factors of the lidar equation cancel. For this it is assumed that the overlap functions are the same. For well aligned systems, this is the case above a certain minimum height. It is also assumed that atmospheric extinction of both signals is the same. Then the temperature dependence of the ratio Q is given by

$$Q(T) = \frac{\sum_{i=\mathrm{O_2,N_2}} \sum_{J_i} \tau_{\mathrm{RR2}}(J_i)\eta_i \left(\dfrac{\mathrm{d}\sigma}{\mathrm{d}\Omega}\right)_{\pi}^{\mathrm{RR},i}(J_i)}{\sum_{i=\mathrm{O_2,N_2}} \sum_{J_i} \tau_{\mathrm{RR1}}(J_i)\eta_i \left(\dfrac{\mathrm{d}\sigma}{\mathrm{d}\Omega}\right)_{\pi}^{\mathrm{RR},i}(J_i)} \tag{10.25}$$

where the formula for the Stokes or anti-Stokes differential backscatter coefficients have to be inserted depending on which branch of the pure RR spectrum is used. $\tau_{\mathrm{RR1}}(J_i)$ and $\tau_{\mathrm{RR2}}(J_i)$ are the transmissions of the lidar receiver at the wavelength of the rotational Raman line J_i. Figure 10.2 shows typical temperature dependencies of the RR signals used for atmospheric temperature measurements.

In order to provide the atmospheric temperature profile, $Q(T)$ must be calibrated. The calibration can be done by characterizing the system parameters and using Eq. (10.25). This approach, however, may yield uncertainties on the order of a few K [44]. In practice, RR temperature lidar is therefore calibrated by comparison with data measured with other instruments such as local radiosondes; the temperature data of today's

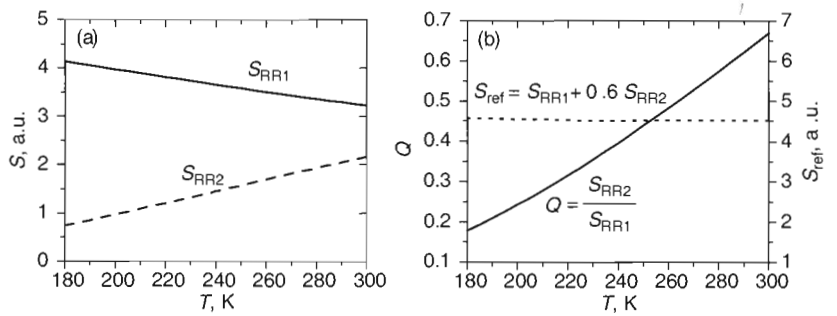

Fig. 10.2. (a) Typical intensities of the two pure-rotational Raman signals S_{RR1} and S_{RR2} as a function of temperature T [48]. (b) Signal ratio Q from which the atmospheric temperature is derived. S_{ref} can be used as a temperature-independent Raman reference signal for measuring extinction and backscatter coefficients of aerosols and cloud particles [47].

state-of-the-art radiosondes are accurate within tenths of a K provided the radiosonde itself has been accurately calibrated. Of course, the reference data used for the calibration should be taken as close in space and time as possible to the atmospheric column sensed by the lidar. How often an RR lidar systems needs to be recalibrated depends on the individual system. Provided that rugged mounts are used and the alignment of the lidar is not changed intentionally, the calibration of today's state-of-art systems remains virtually unchanged and only long-term degradations of the optical components may require recalibrations on a longer time scale.

For systems that detect only one RR line in each of the two RR channels Eq. (10.25) takes the simple form

$$Q(T) = \exp(a - b/T), \tag{10.26}$$

where the parameters a and b are both positive if $J(S_{RR2}) > J(S_{RR1})$. b is simply the difference of the rotational Raman energies of the extracted lines divided by k, and a is the logarithm of the ratio of all factors except the exponential term in Eq. (10.20). It is straightforward to use Eq. (10.26) also for systems with several lines in each of the RR signals [42]. But the obvious inversion of Eq. (10.26) which gives

$$T = \frac{b}{a - \ln Q} \tag{10.27}$$

then turns out to yield significant measurement errors, well in excess of 1 K (cf. Fig. 10.3) when measurements are made over an extended

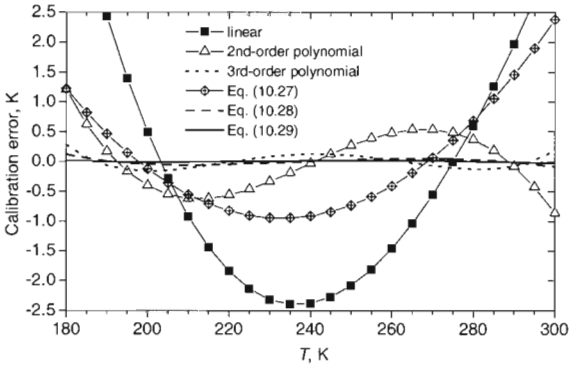

Fig. 10.3. Errors made with different calibration functions for rotational Raman temperature lidar.

range of temperatures. As the errors behave nearly as a second-order-polynomial function of temperature, it has been proposed to minimize calibration errors by a second calibration with such a second-order polynomial [43, 62], leading to a calibration function of the form

$$T = \frac{b}{a - \ln Q} + c\left(\frac{b}{a - \ln Q}\right)^2 + d \tag{10.28}$$

with the additional calibration constants c and d.

An even better calibration function, however, is found in the approach

$$Q = \exp\left(\frac{a'}{T^2} + \frac{b'}{T} + c'\right) \Longleftrightarrow T = \frac{-2a'}{b' \pm \sqrt{b'^2 - 4a'(c' - \ln Q)}}, \tag{10.29}$$

which extends Eq. (10.26) to a second-order term in T and needs only three calibration constants a', b', c'. Fitting, as an example, the curve $T(Q)$ shown in Fig. 10.2 with the different calibration functions, one gets the calibration errors shown in Fig. 10.3. The performances of polynomial calibration functions are also given for comparison. The single-line approach of Eq. (10.27) results here in errors of $\sim\pm 1$ K for temperatures between 180 and 285 K, which is better than a linear calibration function. However, this relation is not generally valid [63]. For three calibration constants, Eq. (10.29) is superior to the second-order polynomial and even better than the third-order polynomial and the approach of Eq. (10.28), which both require four calibration constants. For Eq. (10.29), the temperature derived from the data with that

calibration function differs from the input temperature of the simulation by less than ± 0.03 K for temperatures between 180 and 300 K. With Eq. (10.28) or the third-order polynomial approach, the deviations are about ± 0.10 K and ± 0.15 K, respectively.

In conclusion, when data that cover a large range of temperatures (>50 K) are available for the calibration, Eq. (10.29) is the best-suited calibration of RR temperature lidar when several RR lines are sampled with each channel. Otherwise the single-line approach of Eq. (10.27) should be used to avoid large extrapolation errors.

10.4.3 Technological Considerations

Laser Wavelengths

Because it combines high output power with reliability and ease of handling, the Nd:YAG laser is at present the most widely used light source for Raman lidar systems. We theoretically investigate in the following the performance of RR temperature lidar with frequency-doubled and frequency-tripled radiation of a Nd:YAG laser, i.e., 355 nm and 532 nm. The fundamental emission at 1064 nm is less suitable because of low RR backscatter cross-sections and poorer detector efficiencies at this wavelength. Measurements with the fourth harmonic at 266 nm are limited to short range because light of this wavelength is strongly absorbed by ozone.

The ratio of photon counts in the rotational Raman channels is given by

$$\frac{S_{\mathrm{RR}}(\lambda_1, J)}{S_{\mathrm{RR}}(\lambda_2, J)} = \frac{\mathrm{d}\sigma_J/\mathrm{d}\Omega(\lambda_1)}{\mathrm{d}\sigma_J/\mathrm{d}\Omega(\lambda_2)} \left(\frac{\tau(\lambda_1)}{\tau(\lambda_2)}\right)^2 \frac{K(\lambda_1)}{K(\lambda_2)} \frac{S_0(\lambda_1)}{S_0(\lambda_2)} \tag{10.30}$$

where $S_{\mathrm{RR}}(\lambda_i, J)$ are the numbers of photon counts detected and $S_0(\lambda_i)$ are the numbers of photons transmitted by the lidar. J is the rotational quantum number, $K(\lambda_i)$ denote the receiver efficiencies, $(\mathrm{d}\sigma_J/\mathrm{d}\Omega)(\lambda_i)$ are the differential cross sections for pure rotational Raman backscattering, and $\tau(\lambda_i)$ are the transmissions of the atmosphere with $i = 1, 2$ and the primary wavelengths $\lambda_1 = 532$ nm and $\lambda_2 = 355$ nm. (The atmospheric transmission is approximately constant within the pure rotational Raman spectrum of one primary wavelength.)

The ratio of rotational Raman cross sections is

$$\frac{\mathrm{d}\sigma_J}{\mathrm{d}\Omega}(\lambda_1) \Big/ \frac{\mathrm{d}\sigma_J}{\mathrm{d}\Omega}(\lambda_2) \approx (\lambda_2/\lambda_1)^4 = (2/3)^4 \approx 0.2. \tag{10.31}$$

Ozone absorption is <2% for λ_1 and <0.5% for λ_2 up to 30 km height [63]. So differences in ozone absorption can be neglected and the most important term that depends on height z for this comparison is the atmospheric transmission due to Rayleigh extinction. It is described by

$$\tau_{\mathrm{Ray}}(z) = \exp\left(-\int_{z_0}^{z} N(\zeta)\sigma_{\mathrm{Ray}}(\lambda)d\zeta\right), \tag{10.3}$$

where $N(\zeta)$ is the molecular number density at height ζ. It is taken here from a standard atmosphere. The total Rayleigh cross section can be calculated with

$$\sigma_{\mathrm{Ray}}(\lambda) = \frac{8\pi^3(n(\lambda)^2-1)^2}{3\lambda^4 N_s^2}\left(\frac{6+3\gamma}{6-7\gamma}\right) \tag{10.32}$$

where $\gamma = 0.0279$ is called "depolarization factor," $N_s = 2.547 \times 10^{25}\,\mathrm{m}^{-3}$ is the molecular number density, and n is the refraction index of air (both at standard conditions) with $n(\lambda_1) - 1 = 2.78197 \times 10^{-4}$ and $n(\lambda_2) - 1 = 2.85706 \times 10^{-4}$ [64, 65].

Typical values of the transmissions of the optical components in the receivers and typical detector efficiencies yield a ratio

$$\frac{K(\lambda_1)}{K(\lambda_2)} \approx 2. \tag{10.33}$$

For the same laser power, the ratio of the number of emitted photons is then given by

$$\frac{S_0(\lambda_1)}{S_0(\lambda_2)} = 1.5. \tag{10.34}$$

If laser pulse energies are the same for the two wavelengths, we thus have

$$\frac{P_{\mathrm{RotRam}}(\lambda_1, J)}{P_{\mathrm{RotRam}}(\lambda_2, J)} = 0.6T^*(z) \tag{10.35}$$

with the height-dependent term

$$T^*(z) = (\tau(\lambda_1)/\tau(\lambda_2))^2 \tag{10.36}$$

which describes the effect of atmospheric transmission.

$T^*(z)$ and $S_{\mathrm{RR}}(\lambda_1, J)/S_{\mathrm{RR}}(\lambda_2, J)$ as a function of height are shown in Fig. 10.4. Rotational Raman signals from altitudes above 20 km are ~60% stronger if a primary wavelength of $\lambda_1 = 532$ nm instead of $\lambda_2 = 355$ nm is used. This means that it is advantageous to use 532 nm as the

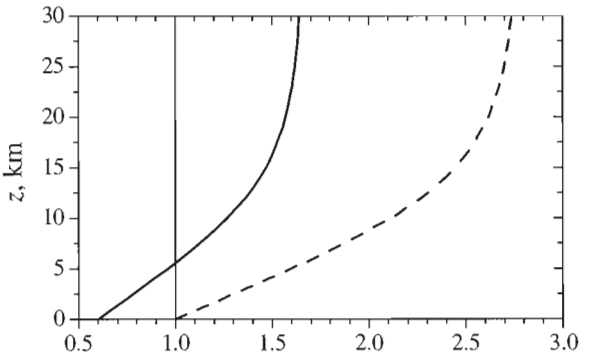

Fig. 10.4. Calculated ratio of rotational Raman signal intensities $S_{RR}(\lambda_1, J)/S_{RR}(\lambda_2, J)$ (solid curve) and atmospheric transmission factor $T^*(z)$ (dashed curve) versus height z with primary wavelengths $\lambda_1 = 532\,\text{nm}$ and $\lambda_2 = 355\,\text{nm}$ for equal laser power (see text for further details).

primary wavelength for a system aiming at high performance in the upper troposphere and in the stratosphere, whereas 355 nm is better suited for temperature measurements in the lower troposphere if the same laser power is available at both wavelengths. These results, however, were obtained under the assumption of Eq. (10.33). With future improvements in receiver technology, this assumption must certainly be reevaluated, which will extend the range for which UV primary wavelengths are superior for RR lidar. First measurements with a system not yet optimized were very promising and have already shown the general feasibility of using 355 nm as the primary wavelength for RR lidar [66].

In addition to signal intensity, it is also important to consider possible differences of the blocking of the elastic backscatter light in the RR channels. The molecular elastic backscatter signal is proportional to λ_0^{-4}, just like the pure rotational Raman signal. Thus no differences in relative signal intensity exist and the relative blocking required for merely the molecular elastic signal is independent of laser wavelength. For particle backscattering, the wavelength dependence varies with size, composition, and shape of the particles. One simplifying rule says that, if the average particle size is significantly larger than both laser wavelength (which is the case for most types of clouds and many types of aerosols), then the relative intensity of the particle signal is lower in the UV than in the visible. There is thus an advantage for a UV primary wavelength under the same atmospheric conditions. On the other hand, the blocking of the elastic backscatter signal in the RR channels that can be achieved today is also lower in the UV which tends to compensate that advantage.

Required Suppression of the Elastically Backscattered Light in the Rotational Raman Channels

The major technical challenge for temperature measurements with the rotational Raman technique is to achieve sufficient blocking of the elastic backscatter signal in the rotational Raman channels. The problem is particularly serious in the low-J channel because of its close proximity ($<30\,\mathrm{cm}^{-1}$ or $<1\,\mathrm{nm}$ at $\lambda = 532\,\mathrm{nm}$). In this section we present a calculation which attenuation is needed. This point has risen considerable controversy in the literature [42, 67]. We show that to ensure measurement errors $<1\,\mathrm{K}$ in clouds up to a backscatter ratio (R_{532}) of 50, a blocking by at least seven orders of magnitude is required. This requirement can be met in practice with today's state-of-the- art optics (see Section 10.5).

The backscatter ratio R_{532} is defined as the ratio of total backscatter intensity to molecular backscatter intensity.* The optical thickness χ of the rotational Raman channels at the primary wavelength λ_0 is

$$\chi = -\log_{10}(\tau(\lambda_0)) \tag{10.37}$$

where $\tau(\lambda_0)$ is the filter transmission. For the calculation, we first simulate the pure rotational Raman signal of air for different temperatures. Then we multiply the spectra with the transmission curves of the receiver channels to get the intensities of the unperturbed rotational Raman signals. The results are used for deriving the calibration function. We add an offset to the unperturbed signals of a single input temperature according to the assumed leakage of the elastic signal. The "measured" temperature is then calculated with the perturbed signals via the calibration function. The leakage measurement error is the difference between the input temperature and the temperature which would be measured with the signals including elastic-signal leakage.

As an example, Fig. 10.5 shows the results of such a calculation for a backscatter ratio $R_{532} = 50$ and input temperatures of 180 K and 250 K and the receiver parameters taken from Ref. 46. The leakage measurement error is zero if the ratio of elastic offset signals is the same

* The backscatter ratio, i.e., the ratio of total backscatter signal to molecular backscatter signal, is not consistently defined in the literature. Depending on the system in use, different receiver spectral widths result in the extraction of different fractions of the pure rotational Raman spectrum (PRRS) for the total backscatter signal. As the PRRS is about 3% of the total molecular backscatter signal the differences, however, are small.

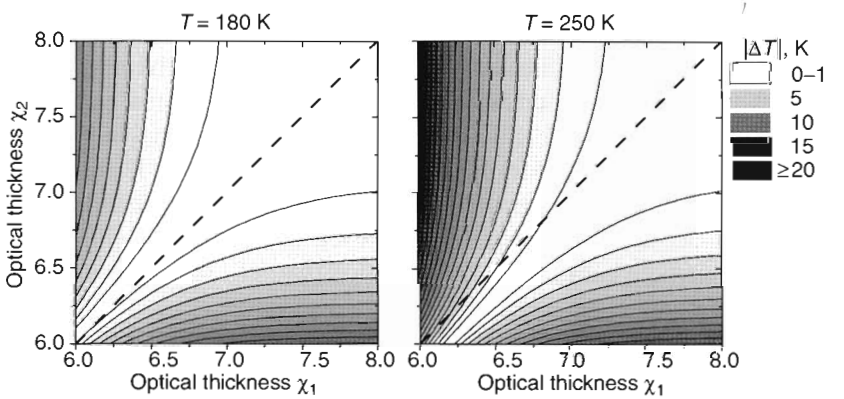

Fig. 10.5. Calculated leakage measurement error ΔT for $R_{532} = 50$ versus the primary-wavelength optical thicknesses χ_1 and χ_2 of the two rotational Raman channels for two "input" temperatures, $T = 180\,\mathrm{K}$ and $T = 250\,\mathrm{K}$. Error contour lines are plotted at intervals of 1 K. Absolute values are given. ΔT is negative in the upper left and positive in the lower right region of the plots. Dashed lines mark $\chi_1 = \chi_2$.

as the ratio of the unperturbed rotational Raman signals. This illustrates directly that the leakage error itself depends on temperature and on the parameters of the individual receiver. If the RR signal intensities are approximately the same within the range of atmospheric temperatures, similar values of elastic backscatter signal blocking are desirable. Ironically, a combination of a lower blocking in one and a higher blocking in the other channel may result in a larger leakage error than the same lower blocking value in both channels.

Figure 10.6 shows leakage errors for equal blocking χ of the two RR channels for different values of "input" temperature. Even if the

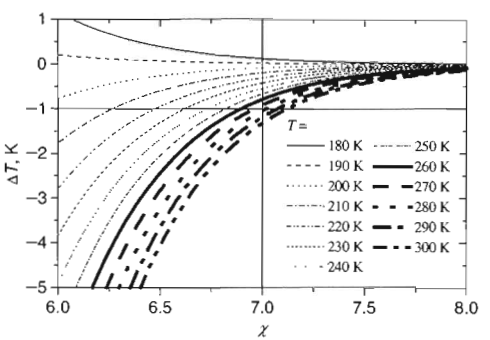

Fig. 10.6. Calculated leakage measurement error ΔT for $R_{532} = 50$ against optical thickness of the two rotational Raman channels $\chi = \chi_1 = \chi_2$ at different temperatures T.

blocking for both RR channels is the same, the sign of the leakage errors is not necessarily the same for all temperatures. With the filter parameters used for this calculation, which may be considered as typical for RR lidar, $|\Delta T|$ is <1 K between 180 and 280 K for $R_{532} = 50$ with $\chi \geq 7$ for both rotational Raman channels. In conclusion, if the elastic backscatter signal is blocked in the RR channels by at least seven orders of magnitude, leakage errors are small even in heights of significantly enhanced particle backscatter signals.

Center Wavelengths and Bandwidths of the RR Channels

Next, we investigate the important question which filter center wavelengths ($\mathrm{CWL_{RR1}}$ and $\mathrm{CWL_{RR2}}$) and channel passbands (full-width-at-half-maximum bandwidths $\mathrm{FWHM_{RR1}}$ and $\mathrm{FWHM_{RR2}}$) yield the minimum statistical temperature error of RR temperature measurements. We can limit the calculations to combinations of the filter parameters with $\mathrm{CWL_{RR1}}$, $\mathrm{CWL_{RR2}}$ in regions of opposite temperature dependence and $\mathrm{FWHM_{RR1}}$, $\mathrm{FWHM_{RR2}}$ sufficiently small that λ_0 is out of the filter transmission band.

The majority of today's RR lidar systems extract parts of only the anti-Stokes branch of the pure rotational Raman spectrum (PRRS) in order to avoid the risk of interference with aerosol fluorescence. In addition, when anti-Stokes signals are extracted and an interference-filter-based receiver is employed, the distance of the filter center wavelengths to the laser wavelength can be increased by increasing the angle of incidence onto the filters. This allows to fine-tune the transmission wavelength when the blocking at the laser wavelength must be increased.

The 1-σ uncertainty of a photon counting signal S follows Poisson statistics and is therefore given by

$$\Delta S = \sqrt{S}, \tag{10.38}$$

which yields, for the uncertainty of the RR temperature measurement,

$$\begin{aligned}\Delta T &= \frac{\partial T}{\partial Q} Q \cdot \sqrt{\frac{1}{S_{\mathrm{RR1}}} + \frac{1}{S_{\mathrm{RR2}}}} \\ &= \left(\frac{\partial S_{\mathrm{RR1}}}{\partial T} \frac{1}{S_{\mathrm{RR1}}} - \frac{\partial S_{\mathrm{RR2}}}{\partial T} \frac{1}{S_{\mathrm{RR2}}} \right)^{-1} \sqrt{\frac{1}{S_{\mathrm{RR1}}} + \frac{1}{S_{\mathrm{RR2}}}},\end{aligned} \tag{10.39}$$

where

$$Q = \frac{S_{\mathrm{RR2}}}{S_{\mathrm{RR1}}} \tag{10.24}$$

is the ratio of the two signals S_{RR1} and S_{RR2} of lower and higher RR quantum-number transition channels. We can approximate the derivatives in Eq. (10.39) with the corresponding differences such that

$$\frac{\partial T}{\partial Q} \approx \frac{T_2 - T_1}{Q(T_2) - Q(T_1)}. \tag{10.40}$$

It is appropriate to use a peak transmission $\tau = 1$ and an out-of-band transmission $\tau = 0$ in this simulation. With the use of, e.g., Gaussian-shaped filter transmission curves to account for the slope of the filter edges, the resulting data would just be smoother, which would neither improve the clarity of the results nor change the conclusions.

Figure 10.7 shows the temperature sensitivity

$$\frac{\partial S}{\partial T} \approx \frac{S(T_2) - S(T_1)}{T_2 - T_1}, \tag{10.41}$$

for different parts of the RR spectrum when $T_1 = 235$ K and $T_2 = 240$ K. For these temperatures, regions with negative sign of $\partial S/\partial T$ are found at center wavelengths between ~530.5 nm and ~534.5 nm and positive

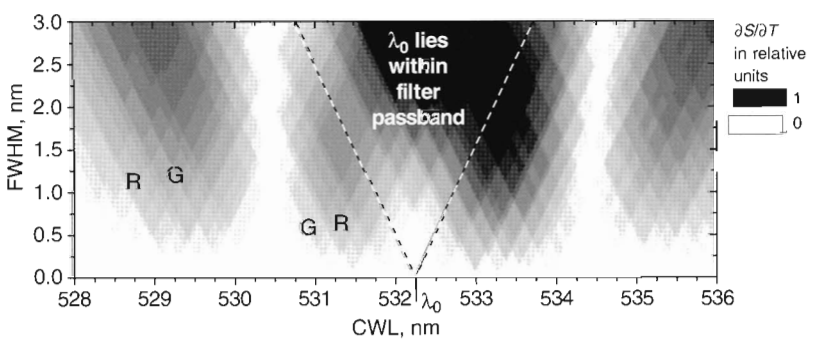

Fig. 10.7. Calculated temperature sensitivity $\partial S/\partial T$ of atmospheric pure rotational Raman signals versus center wavelength CWL and bandpass full width at half maximum FWHM. The laser wavelength λ_0 was set to 532.25 nm, temperatures to $T_1 = 235$ K and $T_2 = 240$ K. Calculation stepwidth was 0.025 nm. Absolute values only are plotted; $\partial S/\partial T$ is negative for CWLs between ~530.5 nm and ~534.5 nm and positive elsewhere. The parameters of two interference-filter-based RR lidars are marked with 'G' [46] and 'R' [48], respectively.

$\partial S/\partial T$ elsewhere. For RR temperature measurements, one RR signal should be taken from each of these regions. Within the data range displayed in Fig. 10.3, the temperature sensitivity of the anti-Stokes signals is most pronounced around ($CWL_{RR1} = 531.30\,nm$, $FWHM_{RR1} = 1.2\,nm$) and ($CWL_{RR2} = 529.30\,nm$, $FWHM_{RR2} = 3.0\,nm$). However, while for the RR1 channel a maximum temperature sensitivity exists because of the boundary imposed by the laser wavelength, the RR2 filter has no such optimum because the extraction of more lines with higher rotational quantum number always improves the sensitivity for this channel. Clearly, it is not the temperature sensitivity alone that must be optimized, but also the intensity of the RR signals, as is described by Eq. (10.39); regions of the RR spectrum with highest signal intensity and highest temperature sensitivity are not identical.

As an example, Fig. 10.8 shows the dependence of the statistical temperature error on filter center wavelengths for filter bandwidths fixed at $FWHM_{RR1} = 0.6\,nm$ and $FWHM_{RR2} = 1.2\,nm$ and for $T_1 = 235\,K$ and $T_2 = 240\,K$. These bandwidths were used by two systems [46, 48] which also meet the requirement of high blocking of the elastic

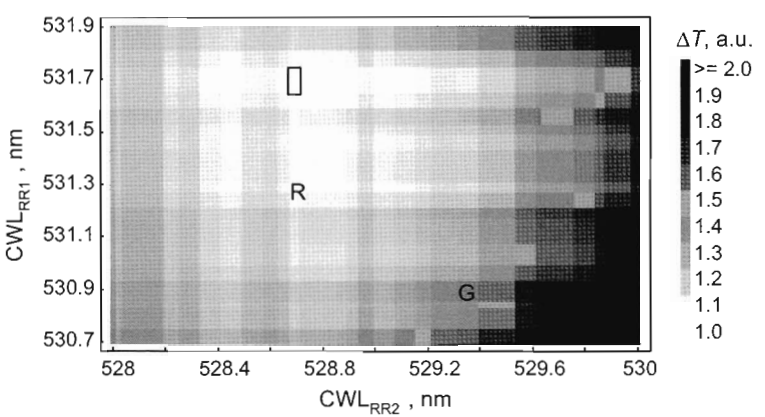

Fig. 10.8. Result of optimization calculations for the center wavelength (CWL) of both rotational Raman channels [48]: Statistical measurement uncertainty ΔT versus filter center wavelengths CWL_{RR1} and CWL_{RR2} for temperatures $T_1 = 235\,K$ and $T_2 = 240\,K$. For the calculation, the filter transmission curves were approximated by rectangular filter passbands with widths of 0.6 and 1.2 nm for the first and second rotational Raman channel, respectively. Calculation step width was 0.025 nm. Values are given relative to the minimum error near $CWL_{RR1} = 531.7\,nm$, $CWL_{RR2} = 528.7\,nm$ (□). 'G' [46] and 'R' [48] mark the CWLs of two RR lidar systems.

backscatter light discussed above. For these temperatures, the statistical temperature error becomes smallest around ($CWL_{RR1} = 531.7$ nm, $CWL_{RR2} = 528.7$ nm).

Optimum filter parameters depend on the temperature that is to be measured. Fortunately this dependence is not very strong within the range of atmospheric temperatures. For example, optimum CWLs for $T_1 = 185$ K and $T_2 = 190$ K, the condensation conditions of polar stratospheric clouds, are 531.70 and 529.35 nm. Using filters optimized for 240 K ($CWL_{RR1} = 531.7$ nm, $CWL_{RR2} = 528.7$ nm) increases measurement uncertainties at 185 K by a mere 10%.

10.5 Technical Implementation: Combined Lidar for Temperature Measurements with the Rotational Raman and the Integration Technique

Because of the high requirements on separation and blocking power of the filters which were only met in recent years, RR temperature lidars have entered the lidar scene at a time when other parameters were already obtained with lidar on a routine basis. It was thus most beneficial that some of these RR lidars could be designed as add-on systems to existing lidar facilities. Many components including the radiation source could thus be shared between the RR and the existing lidar. The system presented in this section as an example for a practical RR temperature lidar is such a combined instrument.

The lidar described in the following was designed for simultaneous temperature measurements with the RR technique and the integration technique at the Radio Science Center for Space and Atmosphere, Kyoto University, Japan [47, 48]. It is not the first instrument combining these techniques [63, 68, 69], but provides the most intense RR signals at the time when this text is written. It may illustrate here the state-of-the-art performance of such a combined system. The RASC lidar is located at the MU (Middle and Upper atmosphere) Radar Observatory at (34.8 °N, 136.1 °E) in Shigaraki, Japan. The receiver scheme for the rotational Raman channels follows a design developed at GKSS Research Center, Germany [46]. The use of narrow-band interference filters allows a consecutive setup of the elastic channel and the two rotational Raman channels. This scheme yields both high efficiency and low cross-talk effects.

A sketch of the RASC lidar is given in Fig. 10.9. The lidar transmitter is an injection-seeded Nd:YAG laser. The seeder wavelength is

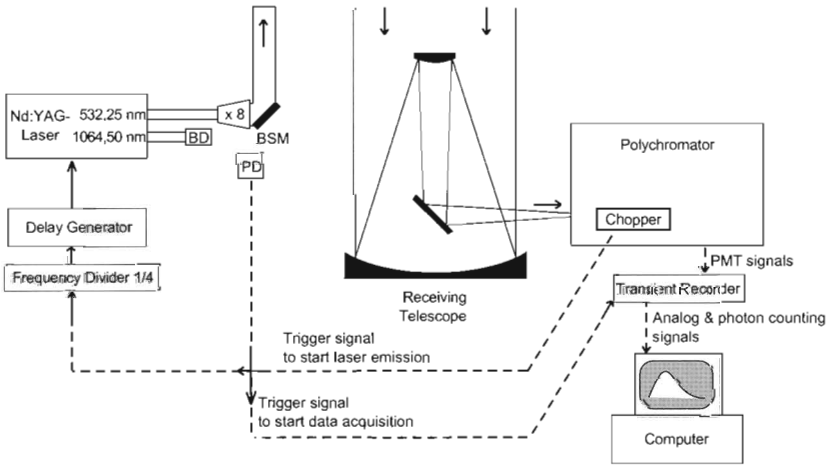

Fig. 10.9. Setup of the RASC lidar. BD beam dump, PD photodiode, BSM beam steering mirror, PMT photomultiplier tube [48].

1064.50 nm in vacuum yielding a wavelength of $\lambda_0 = 532.25$ nm for the second-harmonic radiation which is used as the primary wavelength of the lidar. The laser repetition rate is 50 Hz with an output power of about 30 W at λ_0. Light backscattered from the atmosphere is collected with a Cassegrainian telescope with primary-mirror diameter of 0.82 m. A filter polychromator separates the signals which are finally detected with photomultipiers (PMTs). Data acquisition electronics store the data in both photon counting mode and analog mode with a temporal resolution of typically 3000 laser pulses (1 minute) and a range resolution of 72 m up to a height of 147 km above the lidar, the best possible resolutions in time and height being 10 s and 9 m with the data acquisition system used. The raw data are later smoothed with sliding-average algorithms that are adapted to the requirements of the current atmospheric investigation. The laser emission is synchronized to the mechanical chopper blade which is placed in the branch of the high-altitude elastic channel to protect the PMT from the intense low-altitude signals.

The separation of the elastic signal and the RR signals is done with multi-cavity interference filters (BS3, BS4a, BS4b, and BS5 in Fig. 10.10). The main parameters of the filters are given in Table 10.3. As the reflectivity of each component is near unity for the signals that follow in the line, signal separation is very efficient. In addition, by extracting the elastic signal upstream of the RR signals, the elastic signal intensity in the reflected beam is already attenuated by a factor of 9 when it

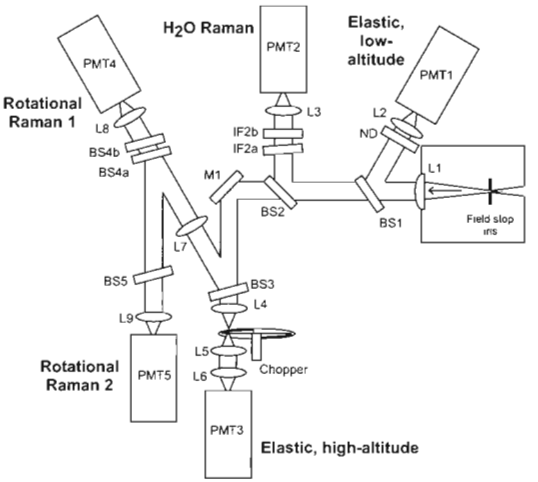

Fig. 10.10. Setup of the RASC lidar polychromator. L1–L9 lenses, IF1–IF2b interference filters, BS1–BS5 beamsplitters, ND neutral density attenuator, PMT1–PMT5 photomultiplier tubes for the signals indicated [48].

reaches the RR channel filters. This feature enhances the elastic-signal blocking for the RR channels and reduces the requirements for the filters used to extract the RR signals. A total receiver blocking of seven orders of magnitude, which was aimed at (see Subsection 10.4.3), is indeed reached. BS3 to BS5 are mounted at small angles of incidence of 4.8°, 5.0°, and 7.2°. By changing these angles the center wavelengths of the extracted signals can be tuned, e.g., to optimize the blocking

Table 10.3. Properties of the beamsplitters BS3, BS4a, BS4b, and BS5 used in the receiver of the RASC lidar. The laser emission, peak transmission of BS4a and BS4b, and peak transmission of BS5 are at the wavelengths of 532.25 nm, 531.1 nm, and 528.5 nm, respectively. AOI angle of incidence, CWL center wavelength, FWHM full width at half maximum, τ transmission, ρ reflectivity.

Parameter	Wavelength, nm	BS3	BS4a & BS4b combined	BS5
AOI, degrees		4.8	5.0	7.2
CWL, nm		532.34	531.14	528.76
FWHM, nm		0.80	0.65	1.10
Transmission/ reflection at	532.25	$\tau = 0.82$, $\rho = 0.11$	$\tau < 10^{-6}$	$\tau < 10^{-6}$
wavelength	531.1	$\rho > 0.95$	$\tau = 0.72$	$\tau < 2 \cdot 10^{-4}$
	528.5	$\rho > 0.96$	$\rho > 0.96$	$\tau = 0.87$

at the laser wavelength or to improve the receiver performance for measurements at varying temperature ranges of interest.

The elastic signal from low altitudes is too intense to be detected in photon counting mode with PMT 3. But that is no problem for low-altitude data alone: If the PMT is not protected from the intense low-altitude radiation, the signals also from higher altitudes are affected by signal-induced noise. Thus a chopper with 100 Hz rotation frequency is employed. The beam is focused on the outer edge of the blade opening at a distance of about 5 cm from the center to allow fast "switching." As the elastic signal from low altitudes is blocked at PMT 3, it is detected in a separate branch with PMT 1. A glass plate (BS1) reflects a small fraction of the total signal intensity out of the beam. The two RR signals of different temperature-dependence are used for both atmospheric temperature measurements and to derive a temperature-independent Raman reference signal. This signal serves to measure the particle extinction coefficient and the particle backscatter coefficient with smaller errors that can be done with the common vibrational Raman technique [47]. The RASC lidar also detects the vibration–rotation Raman signal from water vapor for the measurement of the water vapor mixing ratio. Combining these data with the measured temperature profile yields relative humidity.

The intensities of the rotational Raman signals of the RASC lidar are shown in Fig. 10.11 for typical clear-sky conditions except for a thin cirrus. The RR signals are factors of ~2500 (RR1) and ~5000 (RR2) less intense than the elastic signal. Nevertheless, they allow RR lidar temperature measurements with high resolution both day and night. For a solar elevation angle of 45 degrees, e.g., the 1-σ statistical uncertainty is 1.4 K at a height of 3 km for a measurement resolution of 300 m in 6 minutes with a receiver field-of-view of 1 mrad full-angle [47]). The high blocking of the strong elastic backscatter signal for the Raman channels allows also measurements in thin clouds. No cross-talk is seen up to a backscatter ratio of ~45. Even when cross-talk is found, this does not render the RR data useless. The amount of leakage can be quantified and the leaked-through elastic signals can be subtracted from the apparent RR channel signals [47].

10.5.1 State-of-the-Art Performance

A temperature profile measured with the RASC lidar is shown in Fig. 10.12. The height ranges of the RR data and the integration technique

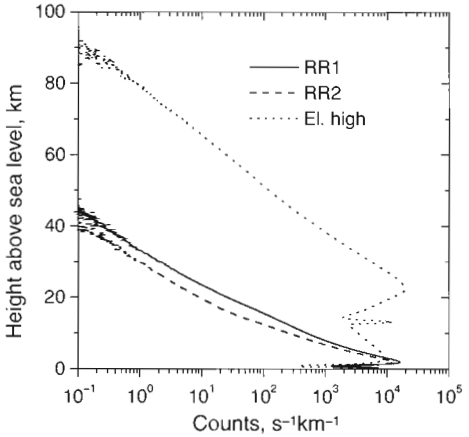

Fig. 10.11. Intensities of the RASC lidar signals for the temperature measurements: rotational Raman signals (RR1 and RR2) and high-altitude elastic signal (El. high). For this plot, 72 minutes (216,000 laser pulses) of nighttime lidar data were taken with a height resolution of 72 m, summed, the background was subtracted, and the data were finally smoothed with a sliding average of 360 m. The photon emission rate of the laser is $\sim 8 \times 10^{19}$ photons/s. In the high-altitude elastic signal, the effect of the chopper can be seen below ~25 km and the signature of a cirrus cloud in ~13 km height.

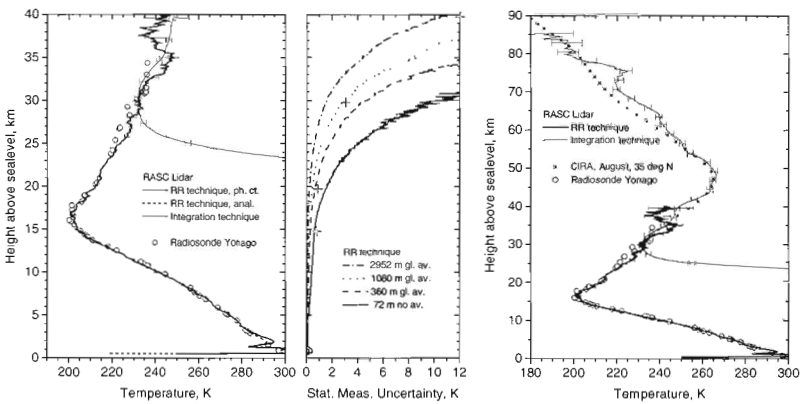

Fig. 10.12. Simultaneous temperature measurements with rotational Raman technique and with integration technique (signals see Fig. 10.11). Profiles of a climatological model atmosphere (CIRA-86 for 35°N and the month of the lidar measurements) and of a radiosonde are shown for comparison. Rotational Raman temperature data: height resolution of 72 m up to 15 km height, 360 m between 15 and 20 km height, 1080 m between 20 and 30 km height, and 2952 m above 30 km. Height resolution of the integration technique data is 2952 m. Error bars show the $1-\sigma$ statistical uncertainty of the measurements [48].

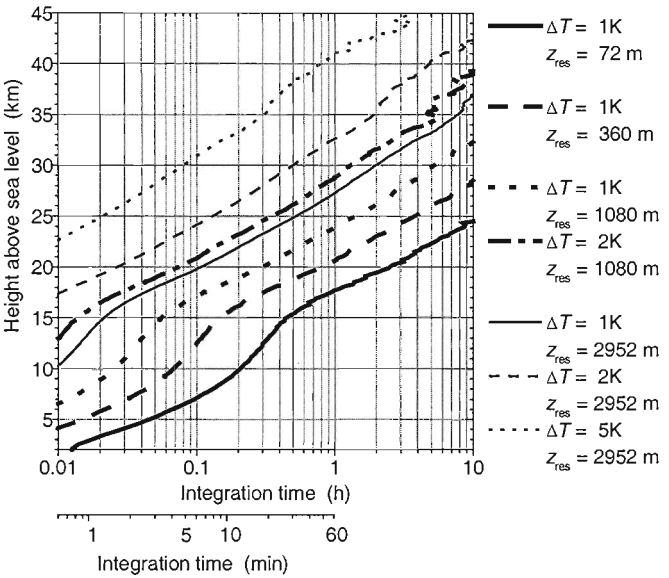

Fig. 10.13. Relation between integration time, height resolution, and statistical uncertainty of the temperature measurements with rotational Raman technique for the RASC lidar (calculated with the same data as those used for Fig. 10.11) [48].

data overlap well. In the overlap region, the results of the two techniques coincide within the statistical uncertainty. At heights below ~29 km the chopper attenuates the signal and interferes with the integration-technique data. The RR temperature data below ~3 km are affected by the nonlinearity of the photon counting electronics (although the signals were corrected for deadtime effects using the model of a nonparalizable detector); here the analog data remain reliable down to ~2 km above sea level which is ~1.6 km above the lidar. For lower altitudes, the overlap geometry between the laser beam and the field of view of the telescope is different for the two RR channels and causes deviations with this system. For measurements at low altitudes a coaxial arrangement of the outgoing laser beam with the receiving telescope would be the preferred geometry to allow measurements from close to the ground upward.

The relation between integration time, height resolution, and statistical uncertainty of the RR temperature measurements of the RASC lidar can be seen in Fig. 10.13. With, e.g., 5 minutes integration time and a

height resolution of 72 m, the $1-\sigma$ statistical uncertainty of the data is <1 K up to $\sim$7 km altitude. For measurements in the stratosphere, e.g., at 23 km altitude an integration time of 1 hour results in 1 K uncertainty for 1080 m averaging, while for 45 km altitude and 2952 m smoothing 4 hours of integration time yield 5 K uncertainty.

This example as well as many of the applications briefly mentioned in Subsection 10.4.1 show that rotational Raman lidar is probably the most accurate, most precise and cheapest method for the determination of vertical profiles of atmospheric temperature in the troposphere and lower stratosphere with or without the presence of aerosols and optically thin clouds. For measuring the temperature in greater heights, a Rayleigh integration lidar is ideally used. Both techniques can be combined in one system. It need not transmit at more than one wavelength. The minimum height of the measurements depends on the overlap between the transmitter and receiver of the system, whereas the measurement resolution and the maximum height of the measurements depend on the transmitted laser power and the size of the receiving telescope. With favorable transmission of the atmosphere such a combined system allows continuous temperature measurements simultaneously in the troposphere, stratosphere and mesosphere.

Acknowledgement

Beneficial discussions with U. Wandinger and T. Leblanc during the preparation of this chapter are gratefully acknowledged.

References

[1] A. Ansmann, U. Wandinger, M. Riebesell, et al.: Appl. Opt. **31**, 7113 (1992)
[2] A. Behrendt, T. Nakamura: Opt. Express **10**, 805 (2002). http://www. opticsinfobase.org/abstract.cfm?id = 69680
[3] V. Sherlock, A. Hauchecorne, J. Lenoble: Appl. Opt. **38**, 5816 (1999)
[4] R.G. Strauch, V.E. Derr, R.E. Cupp: Appl. Opt. **10**, 2665 (1971)
[5] W.P.G. Moskowitz, G. Davidson, D. Sipler, et al.: In *14 International Laser Radar Conference/14 Conferenza Internazionale Laser Radar. Conference Abstracts, Innichen—San Candido, Italy, June 20–23, 1988.* L. Stefamutti, ed., p. 284
[6] P. Keckhut, M.L. Chanin, A. Hauchecorne: Appl. Opt. **29**, 5182 (1990)
[7] J.W. Hair, L.M. Caldwell, D.A. Krueger, et al.: Appl. Opt. **40**, 5280 (2001)

[8] F.A. Theopold, J. Bösenberg: J. Atmos. Ocean. Tech. **10**, 165 (1993)
[9] T. Leblanc, I.S. McDermid, A. Hauchecorne, et al.: J. Geophys. Res. **103**, D6, 6177 (1998)
[10] A. Hauchecorne, M.L. Chanin: Geophys. Res. Lett. **7**, 565 (1980)
[11] L. Elterman: Phys. Rev. **92**, 1080 (1953)
[12] L. Elterman: J. Geophys. Res. **58**, 519 (1953)
[13] L. Elterman: J. Geophys. Res. **59**, 35 (1954)
[14] G.S. Kent, R.W.H. Wright: J. Atmos. Terr. Phys. **32**, 917 (1970)
[15] G. Fiocco, G. Beneditti-Michelangeli, K. Maischberger, et al.: Nature (London) Phys. Sci. **229**, 78 (1971)
[16] R.L. Schwiesow, L. Lading: Appl. Opt. **20**, 1972 (1981)
[17] M.L. Chanin, A. Hauchecorne: J. Geophys. Res. **86**, C10, 9715 (1981)
[18] T. Shibata, M. Kobuchi, M. Maeda: Appl. Opt. **25**, 685 (1986)
[19] R. Wilson, M.L. Chanin, A. Hauchecorne: Geophys. Res. Lett. **17**, 1585 (1990)
[20] R. Wilson, M.L. Chanin, A. Hauchecorne: J. Geophys. Res. **96**, 5153 (1991)
[21] R. Wilson, M.L. Chanin, A. Hauchecorne: J. Geophys. Res. **96**, 5169 (1991)
[22] N.J. Mitchell, L. Thomas, A.K.P. Marsh: Ann. Geophysicae **9**, 588 (1991)
[23] A. Hauchecorne, M.L. Chanin: J. Atmos. Terr. Phys. **44**, 577 (1982)
[24] A. Hauchecorne, M.L. Chanin: J. Geophys. Res. **88**, 3843 (1983)
[25] S.T. Gille, A. Hauchecorne, M.L. Chanin: J. Geophys. Res. **96**, 7579 (1991)
[26] P.D. Dao, R. Farley, X. Tao, et al.: Geophys. Res. Lett. **22**, 2825 (1995)
[27] P. Keckhut, M.E. Gelman, J.D. Wild, et al.: J. Geophys. Res. **101**, D6, 10,299 (1996)
[28] T. Leblanc, I.S. McDermid, D.A. Ortland: J. Geophys. Res. **104**, 11,917 (1999)
[29] T. Leblanc, I.S. McDermid, D.A. Ortland: J. Geophys. Res. **104**, 11,931 (1999)
[30] A. Hauchecorne, M.L. Chanin, R. Wilson: Geophys. Res. Lett. **14**, 933 (1987)
[31] T.J. Duck, D.P. Sipler, J.E. Salah, et al.: Geophys. Res. Lett. **28**, 3597 (2001)
[32] P. Keckhut, M.L. Chanin: Geophys. Res. Lett. **19**, 809 (1992)
[33] M.L. Chanin, N. Smirnes, A. Hauchecorne: J. Geophys. Res. **92**, 933 (1987)
[34] P. Keckhut, M.L. Chanin: *Handbook for MAP (Middle Atmosphere Program)* **29**, 33 (1989)
[35] M.L. Chanin, A. Hauchecorne, N. Smirnes: *Handbook for MAP (Middle Atmosphere Program)* **16**, 305 (1985)
[36] M.L. Chanin, A. Hauchecorne, N. Smirnes: Adv. Space Res. **10**, 211 (1990)
[37] A. Hauchecorne, M.L. Chanin, P. Keckhut: J. Geophys. Res. **96**, 15297 (1991)
[38] P. Keckhut, A. Hauchecorne, M.L. Chanin: J. Atmos. Ocean. Tech. **10**, 850 (1993)
[39] J. Cooney: J. Appl. Meteorol. **11**, 108 (1972)
[40] J. Cooney, M. Pina: Appl. Opt. **15**, 602 (1976)
[41] R. Gill, K. Geller, J. Farina, et al.: J. Appl. Meteorol. **18**, 225 (1979)
[42] Yu.F. Arshinov, S.M. Bobrovnikov, V.E. Zuev, et al.: Appl. Opt. **22**, 2984 (1983)
[43] D. Nedeljkovic, A. Hauchecorne, M.L. Chanin: IEEE Trans. Geo. Rem. Sens. **31**, 90 (1993)
[44] G. Vaughan, D.P. Wareing, S.J. Pepler, et al.: Appl. Opt. **32**, 2758 (1993)
[45] C.R. Philbrick: In *Atmospheric Propagation and Remote Sensing III*, W.A. Flood and W.B. Miller, eds., Proc. SPIE **2222**, 922 (1994)
[46] A. Behrendt, J. Reichardt: Appl. Opt. **39**, 1372 (2000)

[47] A. Behrendt, T. Nakamura, M. Onishi, et al.: Appl. Opt. **41**, 7657 (2002)
[48] A. Behrendt, T. Nakamura, T. Tsuda: App. Opt., **43**, 2930 (2004)
[49] J. Zeyn, W. Lahmann, C. Weitkamp: Opt. Lett. **21**, 1301 (1996)
[50] Yu.F. Arshinov, S.M. Bobrovnikov: Appl. Opt. **38**, 4635 (1999)
[51] W. Lahmann, J. Zeyn, C. Weitkamp: In *Advances in Atmospheric Remote Sensing with Lidar. Selected Papers of the 18th International Laser Radar Conference (ILRC), Berlin, 22–26 July 1996*. A. Ansmann, R. Neuber, P. Rairoux, U. Wandinger, eds. (Springer, Berlin 1997), p. 345
[52] S.M. Bobrovnikov, Yu.F. Arshinov, I.B. Serikov, et al.: In *Lidar Remote Sensing in Atmosphere and Earth Sciences. Reviewed and revised papers presented at the twenty-first International Laser Radar Conference (ILRC21), Québec, Canada, 8–12 July 2002*. L.R. Bissonnette, G. Roy, G. Vallée, eds. (Defence R&D Canada Valcartier, Val-Bélair, QC, Canada), Part 2, p. 717
[53] A. Behrendt, J. Reichardt, A. Dörnbrack, et al.: In *Polar Stratospheric Ozone: Selected Papers of the Fifth European Workshop on Stratospheric Ozone, 26 September–1 October 1999*. G. Amanatidis, J. Pyle, eds. (St. Jean de Luz, France 2000), p. 149
[54] F. Fierli, A. Hauchecorne, B. Knudsen: J. Geophys. Res. **106**, D20, 24,127 (2001)
[55] C.M. Penney, M. Lapp: J. Opt. Soc. Am. **66**, 422 (1976)
[56] R.J. Butcher, D.V. Willetts, W.J. Jones: Proc. Roy. Soc. Lond. A. **324**, 231 (1971); replace in formula (8), p. 238, 2 by 3 as exponent
[57] M. Penney, R.L. St. Peters, M. Lapp: J. Opt. Soc. Am. **64**, 712 (1974)
[58] D.L. Renschler, J.L. Hunt, T.K. McCubbin, et al.: J. Mol. Spectrosc. **31**, 173 (1969)
[59] I.D. Ivanova, L.L. Gurdev, V.M. Mitev: J. Mod. Opt. **40**, 367 (1993)
[60] J. Bendtsen, J. Raman Spectrosc. **2**, 133 (1974)
[61] M.A. Buldakov, I.I. Matrosov, T.N. Papova: Opt. Spectrosc. (USSR) **46**, 867 (1979)
[62] M.L. Chanin, A. Hauchecorne, D. Nedeljkovic: Proc. SPIE **1714**, 242 (1992)
[63] A. Behrendt: *Fernmessung atmosphärischer Temperaturprofile in Wolken mit Rotations Raman-Lidar (Remote sensing of atmospheric temperature profiles in clouds with rotational Raman lidar)*. Doctoral thesis, Universität Hamburg (2000)
[64] L. Elterman: Environmental Research Papers No. 285, Office of Aerospace Research, United States Air Force (1968)
[65] P.M. Teillet: Appl. Opt. **29**, 1897 (1990)
[66] P. Di Girolamo, R. Marchese, D.N. Whiteman, et al.: Geophys. Res. Lett. **31**, L01106, doi:10.1029/2003GL018342 (2004)
[67] J.A. Cooney: Appl. Opt. **23**, 653 (1984)
[68] A. Hauchecorne, M.L. Chanin, P. Keckhut, et al.: Appl. Phys. B **55**, 29 (1992)
[69] U. von Zahn, G. von Cossart, J. Fiedler, et al.: Ann. Geophysicae **18**, 815 (2000)